

See discussions, stats, and author profiles for this publication at: <https://www.researchgate.net/publication/263978410>

# Nucleation, Growth, and Adsorbate-Induced Changes in Composition for Co–Au Bimetallic Clusters on TiO<sub>2</sub>

ARTICLE *in* THE JOURNAL OF PHYSICAL CHEMISTRY C · NOVEMBER 2012

Impact Factor: 4.77 · DOI: 10.1021/jp307888p

CITATIONS

12

READS

14

7 AUTHORS, INCLUDING:



**Randima Piyumalie Galhenage**

University of California, Irvine

8 PUBLICATIONS 33 CITATIONS

SEE PROFILE



**Salai Cheettu Ammal**

University of South Carolina

55 PUBLICATIONS 810 CITATIONS

SEE PROFILE



**Audrey Duke**

University of South Carolina

5 PUBLICATIONS 16 CITATIONS

SEE PROFILE



**Andreas Heyden**

University of South Carolina

63 PUBLICATIONS 2,716 CITATIONS

SEE PROFILE

# Nucleation, Growth, and Adsorbate-Induced Changes in Composition for Co–Au Bimetallic Clusters on TiO<sub>2</sub>

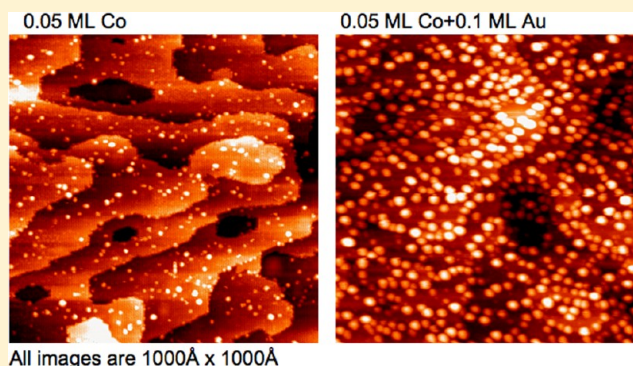
Randima P. Galhenage, Salai C. Ammal,<sup>†</sup> Hui Yan, Audrey S. Duke, Samuel A. Tenney, Andreas Heyden,<sup>†</sup> and Donna A. Chen\*

Departments of Chemistry and Biochemistry and <sup>†</sup>Chemical Engineering, University of South Carolina, Columbia, South Carolina 29208, United States

## S Supporting Information

**ABSTRACT:** The nucleation, growth, and CO-induced changes in composition for Co–Au bimetallic clusters deposited on TiO<sub>2</sub>(110) have been studied by scanning tunneling microscopy (STM), low energy ion scattering (LEIS), X-ray photoelectron spectroscopy (XPS), temperature-programmed desorption (TPD), and density functional theory (DFT) calculations. STM experiments show that the mobility of Co atoms on TiO<sub>2</sub>(110) is significantly lower than of Au atoms; for equivalent or lower coverages of Co, the number of clusters is higher and the average cluster height is smaller than for Au deposition. Consequently, bimetallic clusters are formed by first depositing the less mobile Co atoms, followed by the addition of the more mobile Au atoms.

Furthermore, the reverse deposition of Au followed by Co results in clusters of pure Co coexisting with clusters that are Au-rich. For clusters with a total coverage of 0.25 ML, the cluster density increases and average cluster height decreases as the fraction of Co is increased. Annealing to 800 K results in cluster sintering and an increase of ~3–5 Å in average height for all compositions. LEIS experiments indicate that the surfaces of the bimetallic clusters are 80–100% Au for bulk Au fractions greater than 50%, but Co and Au coexist at the surfaces when there are not enough Au atoms available to completely cover the surfaces of the clusters. After heating to 800 K, pure Co clusters become partially encapsulated by titania, and for bimetallic clusters, the Co is selectively encapsulated at the cluster surface. The desorption of CO from the bimetallic clusters demonstrates that the presence of the CO adsorbate induces diffusion of Co to the cluster surface, but the extent of this diffusion is less than what is observed in the Ni–Au and Pt–Au systems. Density functional theory calculations confirm that for a 50% Co/50% Au bimetallic structure: the surface is predominantly Au in the absence of CO; CO induces diffusion of Co to the cluster surface; and this CO-induced diffusion is less extensive on Co–Au than on the Ni–Au and Pt–Au surfaces.



## INTRODUCTION

The ability to systematically tailor the activity and selectivity of catalytic materials has long been a goal in heterogeneous catalysis. Control over active sites is key to the development of superior catalysts. New active sites can be created on bimetallic surfaces, where electronic modification due to strain effects<sup>1–4</sup> or metal–metal interactions,<sup>2,4–12</sup> the formation of mixed metal sites,<sup>13–15</sup> or other structural changes such as site-blocking<sup>16</sup> gives rise to new chemical activity.<sup>17–21</sup> For example, Chen and co-workers have shown that Pt–Ni bimetallic surfaces exhibit unique chemical activity for a variety of reactions, including hydrogenation of cyclohexene<sup>22–24</sup> and benzene,<sup>23</sup> selective hydrogenation of acrolein,<sup>25</sup> reforming of methanol and ethylene glycol to CO and H<sub>2</sub>,<sup>26</sup> hydrodeoxygenation of *meta*-cresol,<sup>27</sup> and hydrosulfurization of thiophene.<sup>28</sup> A number of DFT studies have also reported that adsorption and dissociation of surface species like H<sub>2</sub>,<sup>2,12,29</sup> O<sub>2</sub>,<sup>12,30</sup> ethylene,<sup>10</sup> CO,<sup>11</sup> and OH<sup>31,32</sup> are different on surface alloys compared to bulk metals. Furthermore, the adsorption of CO is

known to be different on pure metal surfaces compared to thin metal films on metal substrates.<sup>5–7,9</sup> In addition to creating new sites via bimetallic surfaces, interactions between the metal clusters and a reducible oxide support can result in new chemical activity. For instance, an “inverse” catalyst composed of titania clusters supported on Au exhibits the same enhanced activity for the water gas shift reaction as Au clusters supported on titania, illustrating the importance of cluster-support interfacial sites.<sup>33</sup> For supported metal clusters on ceria, oxygen from ceria participates in oxidation processes, forming gaseous products containing lattice oxygen from the ceria support.<sup>34–39</sup> In the three-way catalysts for the conversion of CO, NO<sub>x</sub>, and hydrocarbons into CO<sub>2</sub>, water, and N<sub>2</sub>, the ceria support also plays an important role in oxygen storage.<sup>40–42</sup>

Received: August 8, 2012

Revised: October 4, 2012

Published: October 12, 2012

The Co–Au bimetallic clusters on  $\text{TiO}_2(110)$  present a model system for understanding the nature of metal–metal interactions and metal–support interactions. This study is part of a larger research effort that includes investigations of the growth and activity of Ni–Au and Pt–Au clusters on  $\text{TiO}_2(110)$ ,<sup>43–47</sup> and the behavior of the Co–Au system will be compared. The Co–Au on titania system is of specific interest because it has the potential to serve as an excellent catalyst for the conversion of alcohols to  $\text{H}_2$ . Although Co itself is highly active for C–C and C–H scission in alcohols,<sup>48</sup> decomposition of the alcohol results in the production of CO, which blocks active sites and poisons the catalyst.<sup>49</sup> The oxidation of CO to  $\text{CO}_2$  is known to be catalyzed by Au particles supported on titania,<sup>50–54</sup> and there is strong evidence that this reaction occurs at Au–titania interfacial sites.<sup>54–56</sup> Therefore, the Co–Au bimetallic surfaces could potentially improve conversion of alcohols to  $\text{H}_2$  by providing sites at which the C–C and C–H bonds are cleaved, as well as sites for the removal of CO. Co also has greater selectivity for  $\text{H}_2$  production compared to other catalysts like Pt and Ni due to the ability of Co to suppress the methanation side reaction.<sup>57–61</sup>

Furthermore, the Co–Au bimetallic system exhibits interesting catalytic properties, and there are a number of reactions in which the bimetallic surface has superior activity and selectivity compared to the pure metals. The catalytic activity of Co-based clusters is reported to be improved when the Co is alloyed with noble metals like Au. For example, the activity of Co on a  $\text{TiO}_2$  catalyst used in the Fischer–Tropsch reaction is increased upon the addition of Au,<sup>62</sup> and the same is true for Co on  $\text{Al}_2\text{O}_3$  and  $\text{SiO}_2$ .<sup>63</sup> Moreover, the presence of Au in the Co clusters lowers the temperature at which Co oxide can be reduced,<sup>62–64</sup> and other noble metals such as Ru,<sup>65</sup> Re,<sup>65</sup> and Pt<sup>66</sup> mixed with Co exhibit the same effect. A recent study also reports enhanced activity for Co oxide on Au in the electrochemical evolution of oxygen; specifically, the turnover frequency is  $\sim 40$  times higher for 0.4 ML Co oxide on Au compared to Co on bulk Co oxide.<sup>67</sup> The addition of Au to a kaolin-supported Co catalyst increases the conversion of 1,4-butanediol to 2,3-dihydrofuran, and XRD studies show that the structure of the Co catalyst is modified by the Au.<sup>64</sup> Another example is the addition of Co to an oxide-supported Au catalyst for the gas phase epoxidation of propene using a  $\text{H}_2/\text{O}_2$  mixture.<sup>68</sup> The Co–Au bimetallic clusters are more active for propene oxide formation compared to pure Au, and the bimetallic surfaces are also less susceptible to deactivation compared to pure Au.

In the work reported here, Co–Au bimetallic clusters are grown on rutile  $\text{TiO}_2(110)$  by nucleating Au atoms at existing Co clusters, based on the slower diffusion of Co compared to Au. The resulting cluster surfaces are  $>80\%$  Au for bulk Au fractions of  $>50\%$ , as dictated by the lower surface free energy of Au compared to Co. Although the pure Co clusters are significantly smaller than the Au clusters at room temperature due to the increased nucleation density for Co (5.5 vs 12.7 Å average height), addition of Co to the Au clusters does not suppress cluster sintering. Pure Co clusters become encapsulated by titania upon annealing to 800 K, and for annealed Co–Au clusters, surface Co atoms are selectively encapsulated while the Au atoms remain uncovered. Exposure of the bimetallic clusters to CO results in diffusion of Co to the surface of the clusters, but this effect is less pronounced than what is observed in the Pt–Au and Ni–Au systems. DFT calculations

demonstrate that the CO-induced metal diffusion is thermodynamically driven by the formation of strong CO–metal bonds.

## ■ EXPERIMENTAL SECTION

Experiments were carried out in two ultrahigh vacuum chambers with base pressures below  $5 \times 10^{-11}$  Torr. The first chamber is equipped with a variable-temperature STM (Omicron, VT-25), hemispherical analyzer for XPS and LEIS experiments (Omicron, EA125), and a low energy electron diffraction (LEED)/Auger electron spectroscopy (AES) system (Omicron, SPEC3). The second chamber houses a quadrupole mass spectrometer (Hiden HAL 301/3F) for TPD experiments, a cylindrical mirror analyzer for AES (Omicron, CMA 150) and LEED optics (Specs). Both the first<sup>43,44,47,69–71</sup> and second<sup>44,47,71–73</sup> chambers have been previously described in more detail.

The rutile  $\text{TiO}_2(110)$  crystals (Princeton Scientific Corporation, 1 cm  $\times$  1 cm  $\times$  0.1 cm) were cleaned by  $\text{Ar}^+$  sputtering at 1 kV for 20 min and subsequent annealing to 950–1000 K for 3 min.<sup>44</sup> The resulting crystals were sufficiently conductive for STM as well as electron and ion spectroscopy experiments since this treatment preferentially removed oxygen from the crystal. The crystals were heated via electron bombardment of the Ta backplates,<sup>73,74</sup> and temperatures were monitored by type C or K thermocouples, which were calibrated with an infrared pyrometer.<sup>69</sup> The cleanliness and the order of the  $\text{TiO}_2(110)$ –(1  $\times$  1) surface were confirmed by a combination of STM, XPS, LEIS, LEED, and AES experiments.

In the first chamber, a commercial metal evaporator (Oxford Applied Research, EGC04) was used to deposit metals via heating by electron bombardment; Co (ESPI, 99.995%) was evaporated from a 2 mm diameter rod, and Au was evaporated from pure pellets (Alfa Aesar, 99.95%) housed in a molybdenum crucible. In the second chamber, Au was evaporated by passing current through a tungsten wire cage surrounding a pure Au pellet, and Co was deposited by passing current through a 0.50 mm diameter tungsten wire (ESPI), around which 0.25 mm diameter Co wire (ESPI, 99.995%) was wrapped. Metal fluxes were monitored using a quartz crystal microbalance (Inficon). The quartz crystal microbalance (QCM) was independently calibrated by depositing submonolayer coverages of Au and Pt onto Ru(0001) and imaging with STM to determine the total fraction of the surface covered. The QCM calibration was checked by depositing one monolayer of the metals on  $\text{TiO}_2(110)$  and confirming that the disappearance of the Ti LEIS signal occurred at this coverage. One monolayer (ML) is defined with respect to the packing densities of the Au(111) ( $1.39 \times 10^{15}$  atoms/ $\text{cm}^2$ ) and Co(0001) ( $1.83 \times 10^{15}$  atoms/ $\text{cm}^2$ ) surfaces, respectively. The deposition rate was approximately 0.1 ML/min for both metals.

LEIS experiments were conducted with 600 eV  $\text{He}^+$  ions at a scattering angle of  $130^\circ$ , current to the crystal of 25 nA, step size of 0.2 eV, and dwell time of 0.05–0.2 s. Dwell times were adjusted for each surface in order to use the maximum value that resulted in a  $<10\%$  decrease in the Co and Au signals after seven successive scans. This ensured that the metal signals were not changing due to sputtering effects over the course of heating and acquiring spectra at seven different temperatures. The Au peak was collected over 490–545 eV, while the Co and Ti features were collected over 365–465 eV. A scaled contribution from the Ti peak for clean  $\text{TiO}_2$  was subtracted



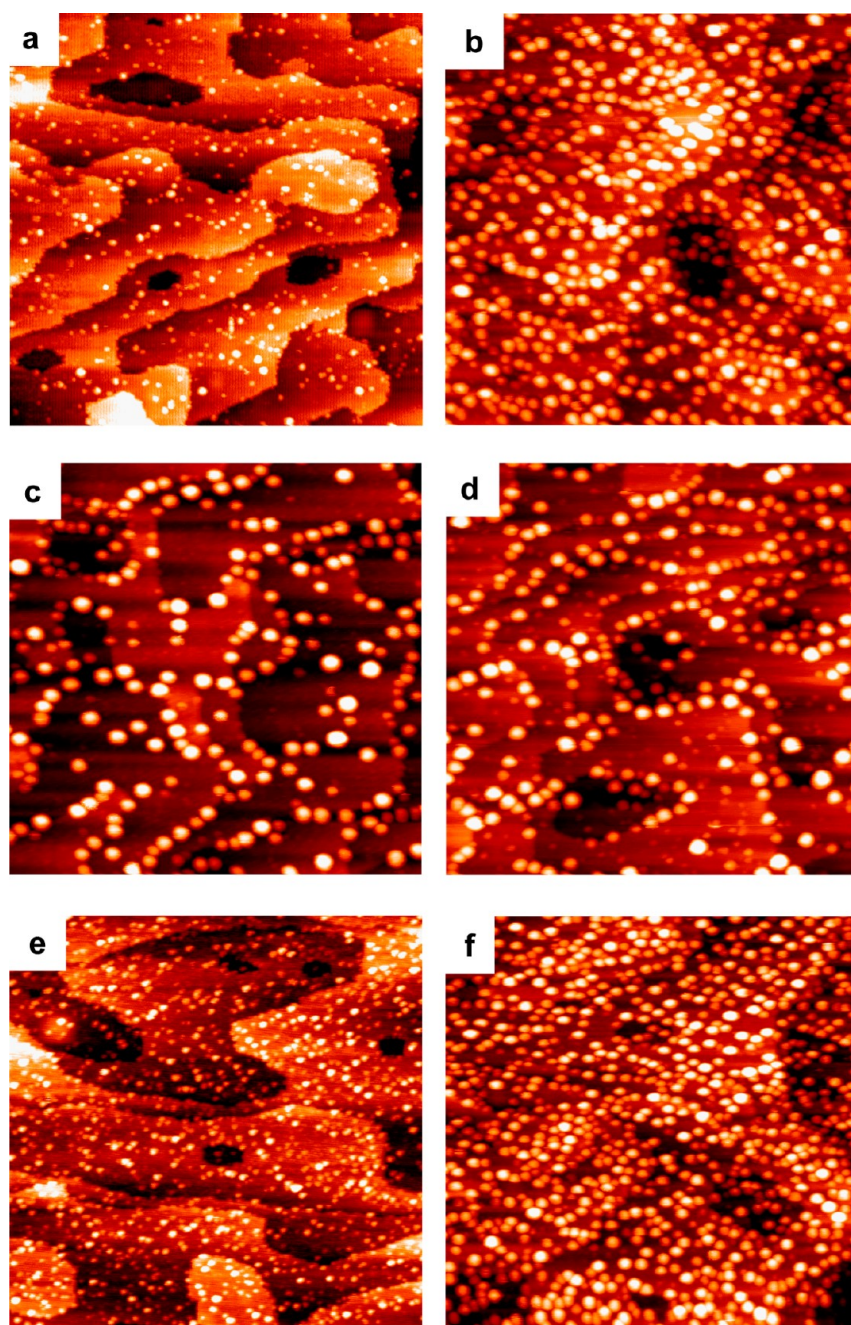


**Figure 1.** STM images of the following metal coverages deposited at room temperature on  $\text{TiO}_2(110)$ : (a) 0.02 ML of Co; (b) 0.02 ML of Co + 0.1 ML of Au; and (c) 0.1 ML of Au; (d) 0.1 ML Au + 0.02 ML of Co; (e) 0.05 ML of Co; and (f) 0.05 ML of Co + 0.1 ML of Au. All images are  $1000 \text{ \AA} \times 1000 \text{ \AA}$ .

from the spectrum in order to generate a flat baseline for integration of the Co peak.

XPS experiments for the  $\text{Co}(2p)$  region were carried out with an  $\text{Al K}\alpha$  anode, a step size of 0.03 eV and dwell time of 0.2 s. For TPD experiments, the crystal was positioned in front of a shielded quadrupole mass spectrometer,<sup>44,71</sup> the heating rate was 2 K/s, and the crystal was biased at  $-100 \text{ V}$  to avoid damage from electrons generated by the mass spectrometer filament. CO (National Welders, 99.99%) was adsorbed onto the surface at 295 K by positioning the crystal  $\sim 2 \text{ mm}$  in front of the end of a stainless steel directed dosing tube and leaking CO into the chamber with a pressure rise of  $3.0 \times 10^{-10} \text{ Torr}$

for 3 min. This exposure resulted in a saturation coverage of CO.

STM experiments were carried out with the sample biased at  $+2.3 \text{ V}$  with respect to the tip using a tunneling current of 0.05 nA–0.1 nA. STM tips were prepared by electrochemically etching 0.38 mm diameter tungsten wire in  $\text{NaOH}$ ,<sup>43</sup> and the tips were conditioned by a combination of  $\text{Ar}^+$  ion sputtering and pulsing to high voltage.

Measurements of cluster heights and surface areas from STM images were conducted with an in-house analysis program that is described in more detail elsewhere.<sup>75</sup> Briefly, this program follows the algorithm developed by Jak et al.<sup>76</sup> to remove steps from the titania surface before automatically measuring cluster

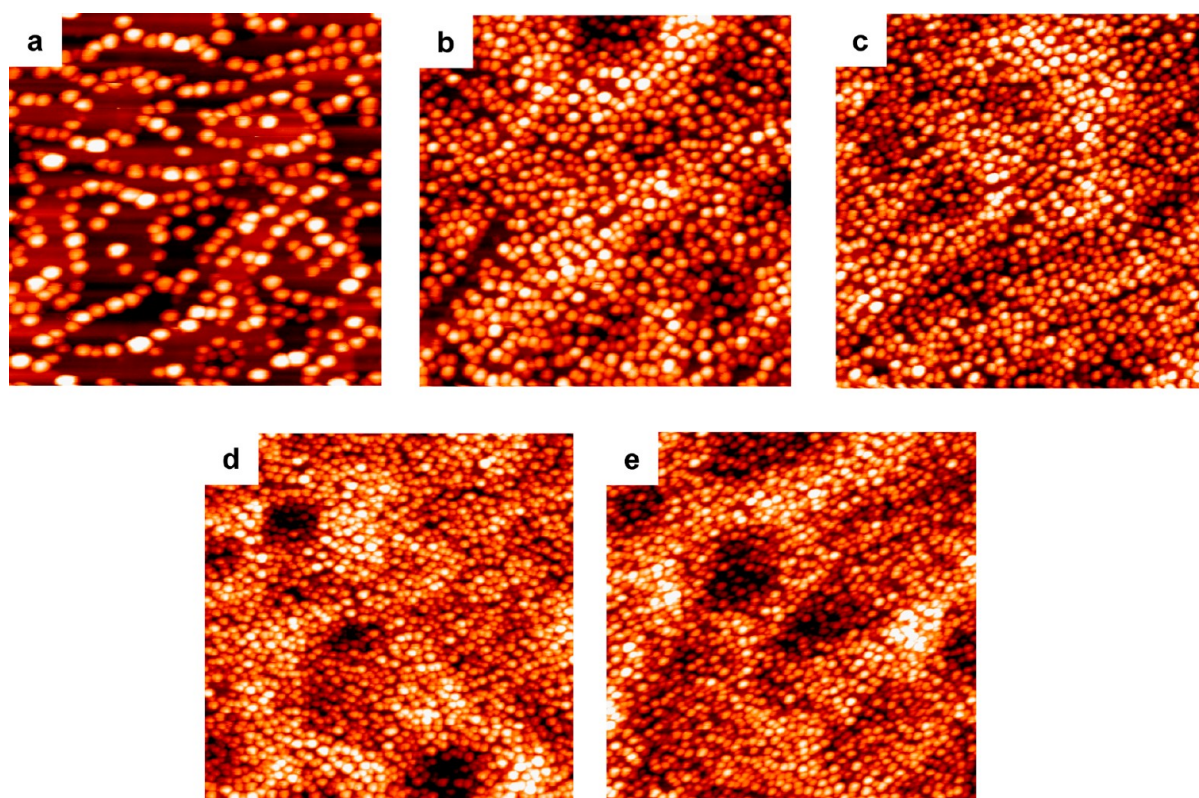


**Figure 2.** STM images of the following metal coverages deposited at room temperature on  $\text{TiO}_2(110)$ : (a) 0.25 ML of Au; (b) 0.06 ML of Co + 0.19 ML of Au; (c) 0.13 ML of Co + 0.13 ML of Au; (d) 0.19 ML Co + 0.06 ML of Au; and (e) 0.25 ML of Co. All images are  $1000 \text{ \AA} \times 1000 \text{ \AA}$ .

heights and diameters. This program also measures the surface area of every cluster in a  $1000 \text{ \AA} \times 1000 \text{ \AA}$  image. Average heights were determined by measuring the heights for clusters in a  $1000 \text{ \AA} \times 1000 \text{ \AA}$  image with the exception of the room temperature 25%Co/75%Au and pure Co surfaces, in which  $1000 \text{ \AA} \times 500 \text{ \AA}$  images containing more than 850 clusters were processed. The reported uncertainties for the room temperature heights are the standard deviations from the cluster height distributions. The reported uncertainties in the cluster densities are the sample standard deviations, which are calculated as the square root of the number of clusters counted and assumes Poisson statistics. Note that the cluster height is taken as the measure of the cluster size since the diameters are known to be overestimated from tip convolution effects.<sup>43</sup> Typically the diameters are overestimated by a factor of 2.2, and this estimate is calculated from an average cluster diameter based on: the total number of atoms deposited as determined by the quartz crystal microbalance, the average cluster height, the number of clusters/ $\text{cm}^2$  and assumes hcp/fcc packing densities for Co and Au. The calculated cluster surface areas were corrected by a factor of  $(2.2)^2$  for the overestimation of the cluster diameters due to tip convolution effects.

## COMPUTATIONAL METHODS

Fully spin-polarized periodic density functional theory (DFT) calculations were performed within the generalized gradient approximation (GGA) using the Vienna ab initio simulation package (VASP).<sup>77–79</sup> The revised Perdew–Burke–Ernzerhof (RPBE)<sup>80,81</sup> functional was used to describe the exchange–correlation effects. A  $(2 \times 2 \times 1)$  Monkhorst-Pack  $k$ -mesh with an energy cutoff of 400 eV was used for all structural relaxations. Energies were calculated with a  $(5 \times 5 \times 2)$   $k$ -mesh.

The Methfessel–Paxton method<sup>82</sup> of order one with a smearing of 0.2 eV was used to allow for partial occupancy near the Fermi level, and dipole corrections to the total energy were computed with Makov and Payne’s modified method.<sup>83</sup> The metal (111) surface was modeled by a  $[3 \times 3]$  supercell with a four-layer slab thickness and a vacuum spacing of 15 Å. Electronic energies were converged to  $10^{-5}$  eV, and ionic relaxations were considered converged when the forces on the ions were less than 0.02 eV/Å. The atoms in the bottom layer of the slab model (typically Au) were fixed to the bulk position of the metal atoms of this layer, and all other atoms were allowed to relax to minimize the total energy. For all bimetallic calculations, the equilibrium lattice constant for bulk Au (4.21 Å) was used; this value was calculated from the RPBE functional with a Monkhorst-Pack  $k$ -point grid of  $11 \times 11 \times 11$ . Co–Au bimetallic structures were obtained by replacing Au atoms with Co atoms at various positions.

## RESULTS

**Scanning Tunneling Microscopy Studies.** STM studies of the sequential deposition of Co and Au at room temperature demonstrate that bimetallic clusters can be formed by depositing the more mobile Au atoms on the less mobile Co. The deposition of 0.02 ML of Co on  $\text{TiO}_2$  results in clusters with average heights of  $3.3 \pm 0.9 \text{ \AA}$  and a cluster density of  $4.8 \pm 0.2 \times 10^{12}/\text{cm}^2$  (Figure 1a). Compared to other metals like Pt,<sup>43,84,85</sup> Rh,<sup>84,85</sup> Ni,<sup>47,86</sup> Cu,<sup>86</sup> Ag, and Au<sup>43,51</sup> on  $\text{TiO}_2(110)$ , Co forms many more nucleation sites as well as smaller average cluster sizes. After the deposition of 0.1 ML of Au on the 0.02 ML Co clusters, there is only a small,  $\sim 6\%$  increase in cluster density up to  $5.1 \pm 0.2 \times 10^{12}/\text{cm}^2$ , indicating that the majority of Au atoms nucleate at existing Co sites (Figure 1b). This is



consistent with the observed increase in average cluster height to  $6.9 \pm 2.8$  Å as the incoming Au atoms are incorporated into Co clusters to form bimetallic clusters. In the absence of Co clusters, the growth of 0.1 ML Au on  $\text{TiO}_2$  (Figure 1c) results in much larger clusters ( $10.0 \pm 3.4$  Å) with a lower cluster density ( $2.1 \pm 0.1 \times 10^{12}/\text{cm}^2$ ), providing further evidence that Au nucleates at the existing Co clusters in Figure 1b. The lower cluster densities for pure Au compared to deposition of pure Co at a coverage five times lower demonstrate that Au is more mobile on the surface than Co. Moreover, the Au clusters are preferentially located at step edges, which are the favored, high coordination sites on the surface, whereas Co clusters nucleate on terraces due to the inability of the Co atoms to diffuse to the step edge sites. For the reverse order of deposition of 0.02 ML of Co on 0.1 ML of Au (Figure 1d), the Co atoms do not nucleate exclusively at Au clusters. After Co deposition, the cluster density increases to  $4.3 \pm 0.2 \times 10^{12}/\text{cm}^2$ , and a bimodal distribution consisting of very small clusters of pure Co ( $\sim 3$  Å) and larger, Au-rich clusters ( $\sim 11$  Å) is observed. Thus, the immobile Co atoms are not always able to diffuse to existing Au clusters, and pure Au and pure Co clusters coexist on the surface along with bimetallic clusters. When 0.1 ML of Au is deposited on a higher Co coverage of 0.05 ML (Figure 1e, f), the cluster density decreases from  $9.2 \pm 0.3 \times 10^{12}$  to  $8.0 \pm 0.3 \times 10^{12}/\text{cm}^2$ . This implies that Au nucleates at Co clusters and that cluster coalescence occurs as the individual clusters grow. When the initial coverage of Co clusters is sufficiently high ( $\geq 0.05$  ML Co) to create a large number of nucleation sites, Au nucleates exclusively at the existing Co clusters.

Given that bimetallic clusters can be formed by the deposition of Co followed by Au, surfaces with varying bimetallic compositions were deposited at room temperature, keeping the total metal coverage fixed at 0.25 ML. The higher metal coverages were employed to increase the number of surface sites for chemical studies on Co–Au bimetallic clusters. Figure 2 shows STM images of clusters with average Co compositions of 0, 25, 50, 75, and 100%, corresponding to 0.25 ML Au, 0.06 ML Co + 0.19 ML Au, 0.13 ML Co + 0.13 ML Au, 0.19 ML Co + 0.06 ML Au and 0.25 ML Co, respectively. The cluster densities as well as the average heights of the clusters are presented in Figure 3 as a function of Co fraction. The nucleation density increases almost linearly with increasing Co fraction. At the highest Co fractions, small clusters appear to cover almost the entire surface, in contrast to the pure Au clusters, which form larger clusters that leave the majority of the titania surface exposed. Likewise, the average cluster heights at room temperature generally decrease with increasing Co fraction since the higher Co coverages provide a larger number of nucleation sites. The largest decrease in average height occurs between the pure Au clusters ( $12.7 \pm 4.3$  Å) and the 25% Co clusters ( $8.1 \pm 2.3$  Å), with the height then dropping more gradually to  $5.5 \pm 1.6$  Å for the pure Co clusters; height distributions are shown in Figure S1a of the Supporting Information.

Changes in surface morphology were studied by STM after heating to 500 and 800 K for 1 min at each temperature to address the effects of cluster sintering. Average heights and cluster densities for the clusters deposited at room temperature and then heated to 500 and 800 K are shown in Figure 3 as a function of bulk Co composition. Upon heating to 500 K, the average cluster heights increase, and the cluster densities decrease, but the effects are relatively minor at all compositions compared to changes after heating at 800 K. At 800 K, the

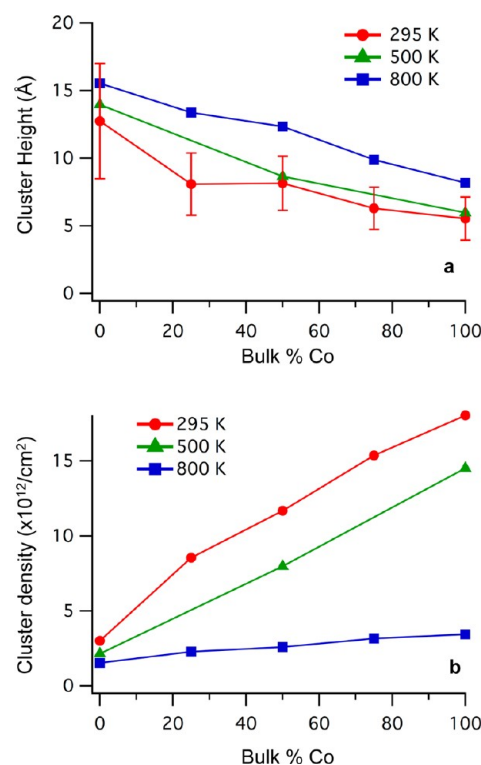


**Figure 3.** Average cluster heights (a) and cluster densities (b) as a function of bulk Co fraction at room temperature and after annealing at 500 and 800 K for 1 min at each temperature. All surfaces have a total metal coverage of 0.25 ML. The error bars shown for the room temperature heights are the standard deviations from the cluster height distributions. Standard deviations for the heights of clusters annealed to 500 and 800 K are not shown for the sake of clarity but are given in Table S1 of the Supporting Information.

number of clusters on the surface is still larger for higher Co fractions, but the decrease in cluster density is only 50% for the pure Au clusters compared to  $\sim 70$ – $80\%$  for all of the Co-containing clusters (Figure 4). This behavior implies that the Co-containing clusters are more easily sintered than pure Au, and the smaller sizes for the 800 K-annealed clusters with high fraction of Co is attributed to the fact that these clusters have significantly smaller heights and higher cluster densities before annealing. For the pure Au clusters, there is a small increase in average cluster height from  $12.7 \pm 4.3$  Å at room temperature to  $15.5 \pm 4.4$  Å after annealing to 800 K. Although the difference in average height is similar for all Co fractions, the height distributions (Figure S1b, Supporting Information) show that the pure Co surfaces annealed at 800 K consist of small clusters with heights of  $\sim 3$  Å in addition to larger clusters of 12–14 Å, and the same is true for the other Co-containing surfaces. For higher Co fractions, the number of  $\sim 3$  Å clusters increases. Thus, the average height is shifted to lower values by the presence of these small clusters and does not reflect the overall increase in cluster size, which is more apparent from the STM images. The appearance of the  $\sim 3$  Å clusters after annealing to 800 K is attributed to small Co clusters that are strongly bound to the  $\text{TiO}_2$  surface, very likely at oxygen vacancy defects, and are therefore not mobile on the surface even at 800 K.

**Low Energy Ion Scattering and X-ray Photoelectron Spectroscopy Studies.** LEIS studies were carried out to characterize the composition of the first monolayer of the

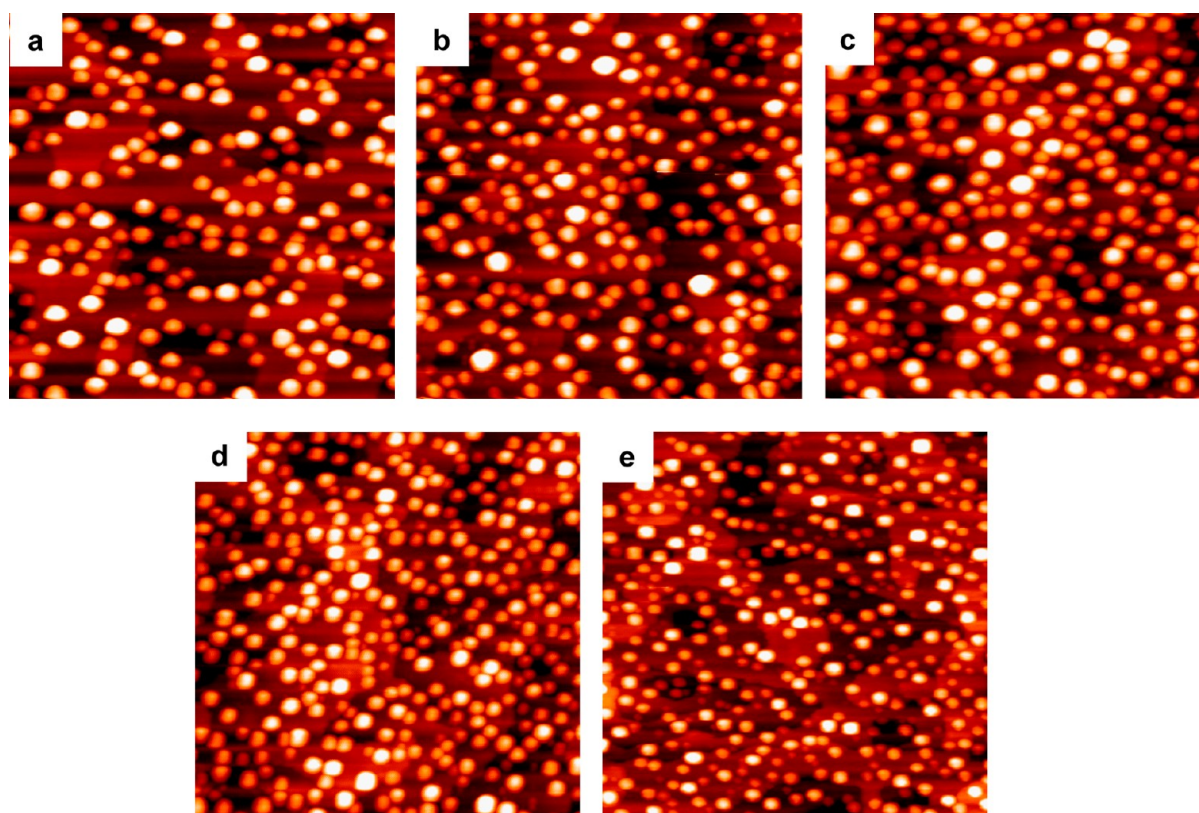


**Figure 4.** STM images of the following metal coverages deposited at room temperature on  $\text{TiO}_2(110)$  and annealed to 800 K for 1 min: (a) 0.25 ML of Au; (b) 0.06 ML of Co + 0.19 ML of Au; (c) 0.13 ML of Co + 0.13 ML of Au; (d) 0.19 ML Co + 0.06 ML of Au; and (e) 0.25 ML of Co. All images are  $1000 \text{ \AA} \times 1000 \text{ \AA}$ .

clusters. Based on the higher surface free energy for Co compared to Au ( $1.9^{87-90}$  vs  $1.1 \text{ J/cm}^{2,88,90}$ ) and the immiscibility of the two metals in the bulk,<sup>91</sup> it is expected that the surfaces of the clusters should be Au-rich when Au is deposited on top of Co seed clusters. The relative sensitivities for Co and Au were determined by depositing 10 ML of Co and 30 ML of Au, collecting LEIS data and determining the surface areas of the two films from STM images.<sup>70</sup> The sensitivity for Au is 3.4 times higher than Co in the LEIS experiment, and for these coverages, no Ti is exposed on the surface. A plot of surface Au composition as determined from LEIS versus the bulk Au % deposited (Figure 5) shows that the clusters are rich in Au (85–100%) for Au fractions greater than 50%. However, it is still possible to prepare clusters with both Co and Au at the surface if the Au fraction is sufficiently low. For example, the clusters with 75% Co/25% Au (0.19 ML Co + 0.06 ML Au) have a surface composition of ~60% Au. A calculation of the total surface area of the 0.19 ML Co clusters from the STM images shows that the deposition of 0.06 ML of Au will leave ~40% of the Co surface exposed because the Au coverage is not high enough to completely cover the Co seed clusters. In contrast, a similar calculation for the 50% Co/50% Au clusters illustrates that 0.13 ML of Au provides sufficient Au atoms to completely cover the 0.13 ML Co seed clusters; the fact that cluster surfaces are ~15% Co at this coverage instead of 100% Au is explained by DFT calculations, which are discussed in a later section.

It is also important to understand compositional changes in the bimetallic clusters that occur upon annealing. When metal clusters such as  $\text{Pt}$ ,<sup>45,84,92</sup>  $\text{Rh}$ ,<sup>84</sup>  $\text{Ni}$ ,<sup>45,47,70,72</sup> and  $\text{Pd}$ <sup>93-95</sup> are heated on  $\text{TiO}_2(110)$  in a reducing environment such as

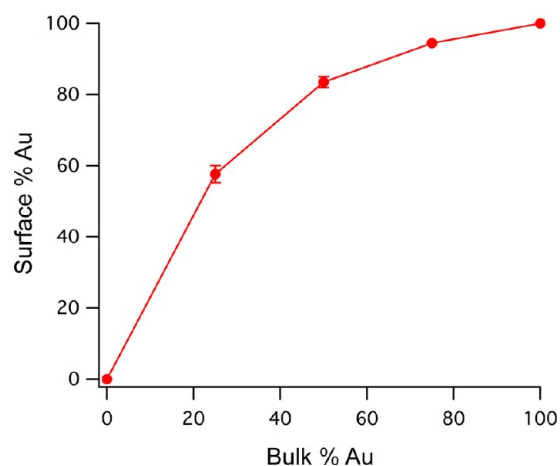


**Figure 5.** Surface % Au from LEIS experiments vs bulk % Au deposited on the surface for Co–Au clusters of varying compositions. The total coverage of all surfaces was 0.25 ML, and Au was deposited on existing Co seed clusters in order to form bimetallic clusters. The error bars shown are the standard deviations from two experiments at 75% Au, three experiments at 25% Au, and four experiments at 50% Au. In the case of 75% Au, the error bar is smaller than the plot symbol.

ultrahigh vacuum (UHV), the clusters become encapsulated by  $\text{TiO}_x$  from the support, and this effect is known as a strong metal support interaction (SMSI).<sup>96-99</sup> It is not known whether Co clusters on titania will also encapsulate upon annealing in UHV, but it is likely that this will occur, given that encapsulation is observed for the neighbors of Co in the



periodic table (Rh, Pd, Ni, Fe).<sup>100</sup> To address the issue of encapsulation, the intensity of the Co LEIS signal was monitored as a function of annealing temperature (Figure 6,

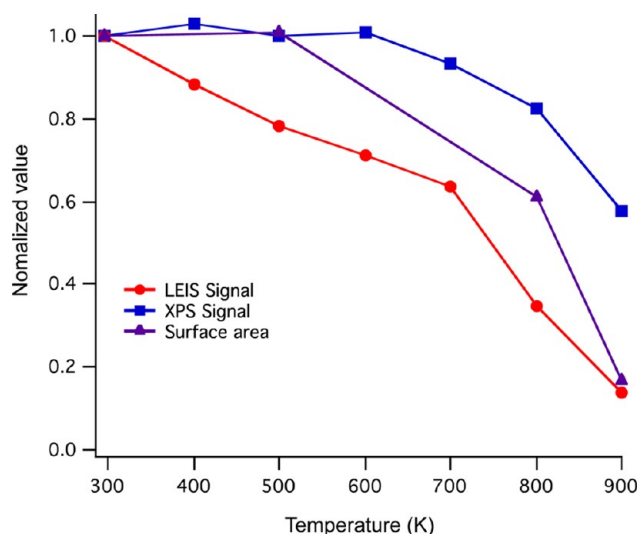


**Figure 6.** Plot of the integrated Co LEIS signal (circles), the integrated Co(2p) XPS signal (squares), and cluster surface area determined by STM (triangles) for 0.25 ML of Co deposited at room temperature and heated to various temperatures for 1 min. All values are normalized to the values at room temperature.

circles). Between room temperature and 700 K, the decrease in Co LEIS signal is almost linear, reaching 64% of the room temperature value at 700 K. Furthermore, at 800 and 900 K, there is a more pronounced decrease in signal, which drops to ~14% of the original value after heating to 900 K. The loss in Co signal can be attributed to one of three processes: encapsulation, decrease in surface area due to sintering and Co desorption. Since the LEIS experiment detects only the top monolayer, the change in surface area determined from STM experiments is also plotted on the same graph in order to help distinguish loss of Co surface area due to sintering versus encapsulation (Figure 6, triangles). After heating to 500 K, there is no change in surface area, but the surface area then drops to 61% and 17% of the initial value at 800 and 900 K, respectively. Although the decrease in surface area and Co LEIS signal is similar at 900 K, the surface area does not diminish as rapidly as the Co LEIS signal at lower temperatures. This implies that the decrease in LEIS signal below 900 K is not solely due to cluster sintering and can be attributed in part to Co encapsulation by titania.

Changes in the XPS Co(2p) intensity for the 0.25 ML Co clusters were also monitored as a function of annealing temperature (Figure 6, squares). Up to 700 K, the decrease in the Co signal is less than 10% compared to the signal at room temperature before annealing. This small loss is assigned to either the onset of encapsulation or decrease in surface area due to sintering. At 800 K, the Co XPS signal decreases to 82% of the value at 295 K, and this is coincident with the substantial reduction in LEIS signal at 800 K. At 900 K, it appears that significant Co desorption occurs; the 43% drop in Co XPS signal from the 295 K value cannot be explained by encapsulation by one or two titania layers, which should attenuate the Co signal by only 9 and 17%, respectively,<sup>101</sup> assuming a mean free path for electrons in titania of 3.47 nm<sup>102</sup>

at a kinetic energy of 708.6 eV for the Co(2p) photoelectrons excited by the Al K $\alpha$  source. Note that XPS is much less sensitive to changes in cluster morphology and surface composition compared to LEIS, given that LEIS probes only the first surface monolayer while XPS probes multiple layers into the near-surface region. For average cluster heights of 6.3 and 11.9 Å at 295 and 800 K, respectively, the Co XPS signal from the clusters should be 74–77% of Co signal for a surface where all of the Co atoms are deposited as a single monolayer; this calculation is based on a mean free path of 14 Å<sup>101</sup> and assumes a hemispherical cluster shape. In summary, it is concluded that the majority of the signal lost at 800 K both in the XPS and LEIS experiments is due to Co encapsulation, whereas Co desorption becomes a significant factor around 900 K.

Changes in both the Co and Au LEIS signals as a function of temperature were studied for the bimetallic clusters of varying compositions with a total metal coverage of 0.25 ML (Figure 7). The normalized Co intensity for the pure Co clusters is shown again to compare directly with the Co signals for the bimetallic clusters (Figure 7a), and all LEIS signals are normalized to the values at room temperature so that relative

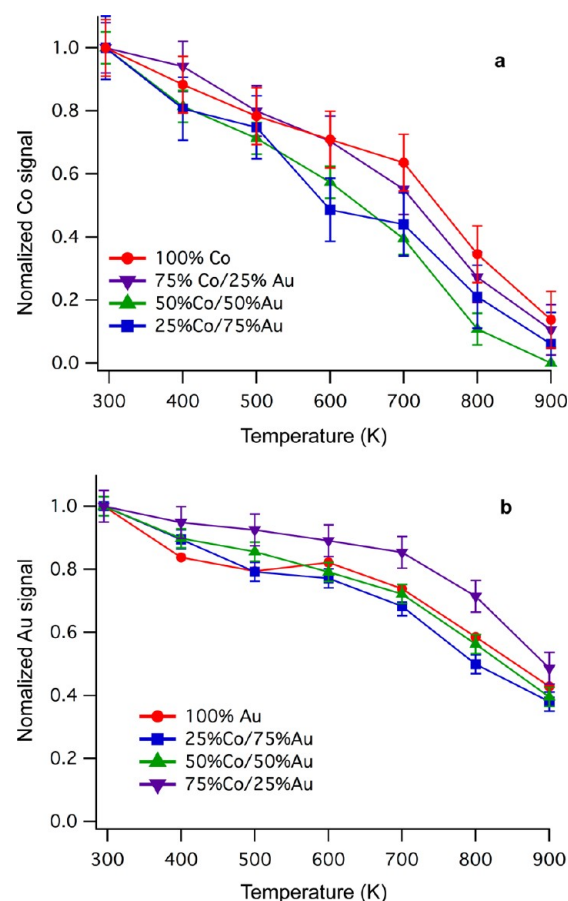


**Figure 7.** LEIS signals as a function of annealing for 1 min at various temperatures for pure Co, pure Au, and Co–Au clusters on TiO<sub>2</sub>: (a) normalized Co signal; and (b) normalized Au signal. Signals are normalized to the initial values at 295 K. Au was deposited on Co clusters at room temperature for various compositions at a total metal coverage of 0.25 ML. The error bars shown are the standard deviations from: two experiments at 75% Au and 100% Co, three experiments at 25% Au, and four experiments at 50% Au. For each composition, the maximum standard deviation in the temperature set was used.



changes can be seen more clearly. For the 75% Co clusters, the decrease in Co signal with annealing temperature closely follows that for the pure Co clusters. Encapsulation is not complete even at 900 K for the 75% Co and pure Co clusters because the Co signal does not drop to zero but remains at 10–15% of the room temperature value. The Co signals for the 50% Co and 25% Co clusters decrease slightly more rapidly than what is observed for the higher Co fractions, but in general the Co signals follow the same general trend: the loss in Co signal is significant at 800 K, and the Co signal decreases almost to zero at 900 K. The data suggest that the reduction in Co signal is greatest for the clusters with lower Co fractions, but given the low absolute signal intensity for the 25% and 50% Co clusters, it is possible that these differences are within experimental error. The normalized Au signal for the pure Au clusters also decreases with annealing temperature, reaching ~60% of the room temperature value at 800 K and ~40% at 900 K (Figure 7b). However, the Au signals for all of the cluster compositions do not drop as quickly as the Co signals. While the 25% Co and 50% Co clusters follow exactly the same trend as the pure Au clusters, the 75% Co clusters have slightly higher values at all temperatures. For example, the decrease in Au signal at 800 K is still ~70% of the room temperature value. This behavior is attributed to the fact that the 75% Co clusters represent the only composition at which there are not enough Au atoms to completely cover the Co surface. When the surface area decreases after cluster sintering at the higher temperatures, all of the Au atoms can still be accommodated at the cluster surface, and therefore, no Au signal is lost due to incorporation of Au atoms into the bulk of the clusters.

**Temperature Programmed Desorption Studies.** Temperature-programmed desorption experiments for CO adsorbed at room temperature were conducted to investigate the surface chemistry on the clusters. Figure 8 demonstrates that CO is evolved (28 amu) from pure 0.25 ML Co clusters in a molecular desorption peak at 370 K and a high temperature peak at 755 K ascribed to recombination of carbon and oxygen atoms from dissociated CO. As the fraction of Au is increased in the 0.25 ML clusters, the CO desorption decreases. Because CO does not adsorb on pure 0.25 ML Au clusters or the  $\text{TiO}_2$  support at room temperature, CO desorption is considered to be a measure of the fraction of Co at the cluster surface. The peak temperature for CO desorption shifts down to 350 K as the concentration of Au is initially increased to 25%, and the peak continues to shift to lower temperature (337 K) at 50 and 75% Au. This behavior suggests that the adsorption energy of CO on Co is decreased when the Co atoms are surrounded by Au atoms instead of Co atoms. Note that the change in desorption temperature cannot be attributed to a CO coverage effect; when the Au fraction is increased, the CO coverage should decrease and induce a shift to higher desorption temperatures as a result of diminished repulsive CO–CO interactions at the lower coverage.<sup>103</sup>

A plot of normalized CO desorption yield and surface composition of Co from the LEIS experiments as a function of bulk Co fraction is shown in Figure 9a. The CO yields are normalized against the value for the pure 0.25 ML Co clusters. Because the normalized CO yield and the fraction of surface Co both have a maximum value of unity at a bulk Co composition of 100%, the relative changes for these two values can be easily compared. The CO desorption yield follows the same general trend as the Co surface composition, but for any given bimetallic composition, the normalized CO yields are ~10%

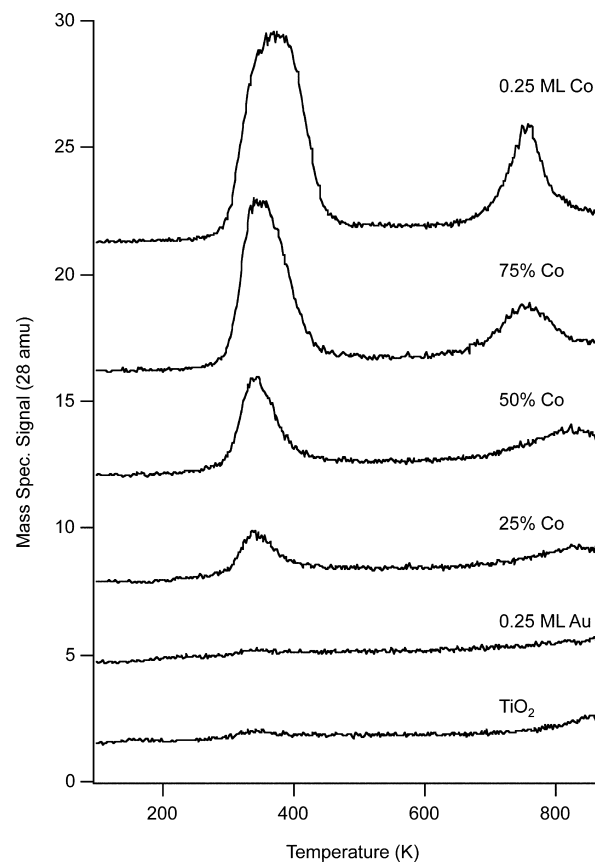


**Figure 8.** TPD experiments for CO adsorbed at room temperature on  $\text{TiO}_2$  itself and on clusters ranging from 0 to 100% Co with a total metal coverage of 0.25 ML. In all cases, the Co was deposited on the surface first, and the heating rate during the TPD experiment was 2 K/s.

higher than the fraction of Co atoms at the surface. Thus, it appears that the strong bonding of CO to Co has a slight effect in inducing the diffusion of Co to the surface. Similar CO-induced diffusion of metals in Ni–Au and Pt–Au clusters have been observed in previous work,<sup>44,47</sup> and these effects are more pronounced for Ni and Pt than for Co (Figure 9b, c), particularly at the 25 and 50% Ni or Pt compositions. In the case of Ni, the normalized CO desorption is 15% and 27% higher than the fraction of Ni at the surface for the 25 and 50% Ni compositions, respectively. In the case of Pt, this difference is even greater, given that the 50% Pt clusters desorb 36% of the CO that is observed from the pure Pt clusters when the fraction of Pt at the surface is essentially zero in the absence of CO. This difference in the ability of CO to extract Co, Ni and Pt from the subsurface layers of the bimetallic clusters is explained by the relative strengths of the CO–metal bonds. The desorption temperatures for a saturation exposure of CO on the pure clusters are 380 K for Co, 400 K for Ni,<sup>47</sup> and 500 K for Pt.<sup>44</sup> The metals with higher CO desorption temperatures form stronger bonds with CO, and CO-induced diffusion of these metals to the cluster surface should occur more readily for the strong metal–CO bonding.

**Density Functional Theory Calculations.** To understand the thermodynamics of Co–Au surfaces in the presence and absence of CO, DFT calculations were carried out on 50% Co/50% Au model surface structures. Four different surface configurations (Figure 10a–d) were considered by substituting

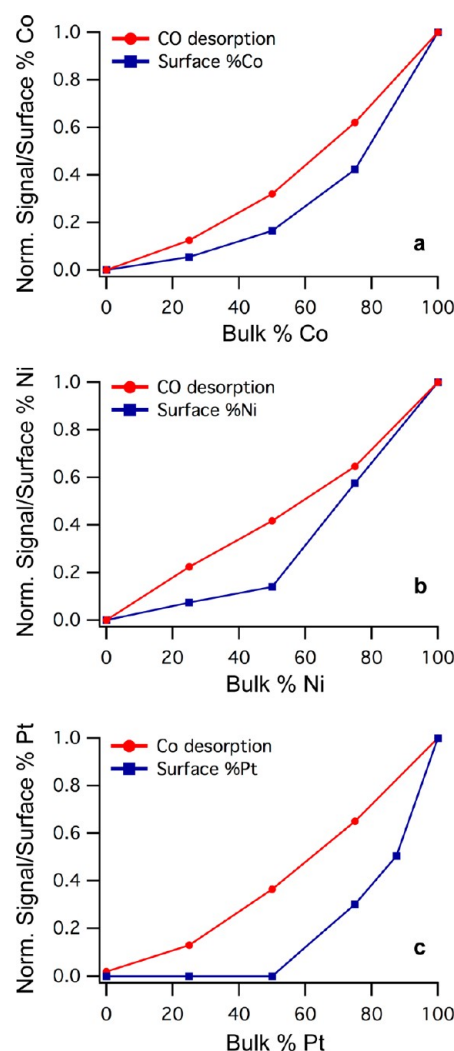


**Figure 9.** Normalized CO desorption yields from TPD experiments and surface % metal from LEIS experiments as a function of bulk % metal deposited on the surface for (a) Co–Au, (b) Ni–Au, and (c) Pt–Au. The CO desorption is normalized to the value on the pure Pt, Ni, or Co clusters. The total coverage of all surfaces was 0.25 ML, and Au was deposited on existing metal seed clusters to form bimetallic clusters. The error bars for the CO yields on Co are the standard deviations from: three experiments on 0.25 ML Co and the 25% Co clusters; two experiments on the 75% Co clusters; and four experiments on the 50% Co clusters.

50% of the Au atoms with Co atoms in the surface model for pure Au. The relative energies ( $E_{\text{rel}}$ ) of these surfaces with respect to the Au-terminated surface model (Au–Co–Co–Au, Figure 10a) are presented in Table 1. Based on these results, Co surface layers are highly unstable compared to Au-terminated surfaces, and this is again consistent with the higher surface free energy of Co ( $1.9 \text{ J/cm}^2$ )<sup>87–90</sup> in comparison to Au ( $1.1 \text{ J/cm}^2$ ).<sup>87,88,90</sup> For the two Co-terminated surfaces, a higher relative energy ( $E_{\text{rel}} = 10.7 \text{ eV}$ ) was calculated for the configuration with alternating layers of Au and Co (Co–Au–Co–Au, Figure 10c). Thus, the immiscibility of the two metals in the bulk results in a preference for two layers of the same metal to cluster together, as in the structure Co–Co–Au–Au (Figure 10b,  $E_{\text{rel}} = 4.3 \text{ eV}$ ). Interestingly, when one Co atom from the third layer is exchanged into the top Au layer for the Au–Co–Co–Au structure (Figure 10d), the energy is decreased by 0.4 eV due to

a better distribution of strain, and therefore, the thermodynamically favored surface is predominantly Au, with a small fraction of Co. This is consistent with the LEIS data, which show that when the Au fraction is high enough for the Au atoms to completely cover the surface of the Co seed clusters, the surfaces are rich in Au (>80%) but still contain some small fraction of Co.

Next, the stability of these structures in the presence of a CO molecule was investigated. CO adsorption was considered at the top site of a Au or Co atom on the four surface models (Figure 10a–d). The relative energies of these surfaces (Table 1) indicate that the Au-terminated surface with one Co atom on the surface (Figure 10e) is the most stable among the four surface models and becomes even more preferred than in the absence of CO due to the strong Co–CO bond. The CO adsorption energies ( $E_{\text{ads}}$ ) given in Table 1 suggest that CO adsorbs more strongly on Co atoms than on Au atoms. However, CO adsorption is weaker by  $\sim 1.5 \text{ eV}$  on Co surrounded by Au atoms (Au(Co<sub>1</sub>)–Co–Co(Au<sub>1</sub>)–Au, Figure 10d) compared to Co surrounded only by Co atoms (Figure 10b). This result is consistent with the TPD data, which demonstrates that the CO desorption temperature is shifted to lower values as the fraction of Au in the clusters is increased. Furthermore, Bader charge analysis indicates that there is a significant amount of charge transfer from Co to the neighboring Au atoms, and the surface Co atom in the Au(Co<sub>1</sub>)–Co–Co(Au<sub>1</sub>)–Au model is positively charged ( $q_{\text{Co}} = +0.33$ ). Thus, back-donation from the positively charged Co metal to the adsorbed CO is reduced ( $q_{\text{CO}} = -0.28$ ), leading to weaker CO adsorption. In comparison, for the Co-terminated surface (Co–Co–Au–Au), the surface Co atoms are nearly charge neutral ( $q_{\text{Co}} = +0.02$ ), resulting in more back-donation of electrons to the adsorbed CO molecule ( $q_{\text{CO}} = -0.40$ ) and a stronger metal–CO bond. Nevertheless, due to the high surface free energy of Co, the stronger CO adsorption is still not sufficient to bring more Co atoms to the surface.

To examine whether additional Co atoms can diffuse to the surface when the CO partial pressure is increased, the phase diagram for a 50% Co/50% Au system was calculated in the presence of CO at a given temperature and CO partial pressure (Figure 11a). Approximate Gibbs free energies are calculated using the following equation:

$$\Delta G = E_{n\text{Co(s)}-n\text{CO}} - E_{1\text{Co(s)}} - n \left( E_{\text{CO}} + \Delta\mu_{\text{CO}}(T, 1 \text{ atm}) + k_{\text{B}}T \ln \left( \frac{P}{1 \text{ atm}} \right) \right) \quad (1)$$

where  $E_{n\text{Co(s)}-n\text{CO}}$  corresponds to a structure with  $n$  Co atoms covered by adsorbed CO on the surface,  $E_{1\text{Co(s)}}$  corresponds to the energy of the most stable surface in the absence of CO (Au(Co<sub>1</sub>)–Co–Co(Au<sub>1</sub>)–Au, Figure 10d),  $\Delta\mu_{\text{CO}}(T, 1 \text{ atm})$  is the (ideal gas) reference chemical potential of CO at temperature  $T$ , and  $P$  is the partial pressure of CO. The calculated phase diagram in Figure 11a suggests that at room temperature and a CO partial pressure of  $10^{-9}$ – $10^{-10}$  atm,  $\sim 11$ – $22\%$  of the surface atoms (1–2 out of 9 surface atoms per unit cell) are Co atoms. A much higher partial pressure of CO ( $10^{-4}$  atm) is necessary to provide sufficient driving force for an  $\sim 33\%$  Co surface composition (3 out of 9 surface atoms per unit cell).

To compare this driving force for metal diffusion to the surface in the Co–Au system with the Ni–Au and Pt–Au

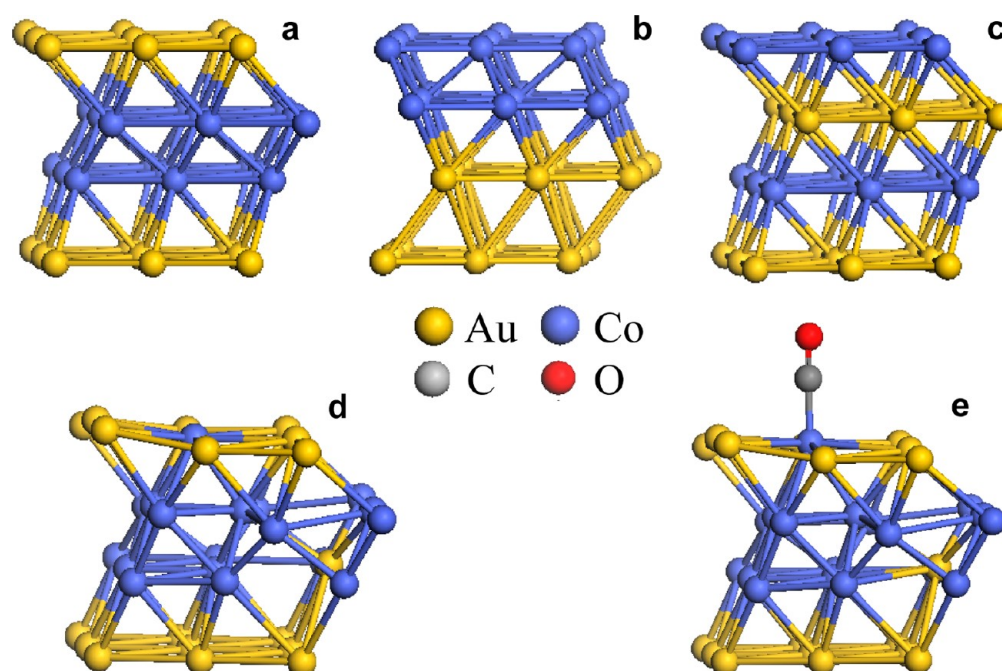


**Figure 10.** Model structures of 50% Co/50% Au surfaces where the bottom Au layer is fixed in bulk Au position: (a) Au–Co–Co–Au; (b) Co–Co–Au–Au; (c) Co–Au–Co–Au; (d) structure (a) with one Co atom exchanged from the third layer; and (e) CO adsorbed on structure (d).

**Table 1.** Computed Relative Energies ( $E_{\text{rel}}$ ) of the 50% Co/50% Au Structures in the Presence and Absence of CO, and Calculated Adsorption Energies ( $E_{\text{ads}}$ ) of CO on These Structures

structure	Co–Au clean surface	CO adsorbed on Co–Au	
	$E_{\text{rel}}$ (eV)	$E_{\text{rel}}$ (eV)	$E_{\text{ads}}$ (eV)
Au–Co–Co–Au (Figure 10a)	0.0	0.0	−0.8
Co–Co–Au–Au (Figure 10b)	4.3	2.4	−2.6
Co–Au–Co–Au (Figure 10c)	10.7	8.3	−3.2
Au(Co <sub>1</sub> )–Co–Co–(Au <sub>1</sub> )–Au (Figure 10d)	−0.4	−0.7	−1.1

systems, the phase diagrams for 50% Ni/50% Au and 50% Pt/50% Au structures were also calculated. A similar computational setup as described above for the Co–Au structures was used for Ni–Au and Pt–Au. The most stable structure in the absence of CO for the latter two systems is the Au-surface terminated structure. The diffusion of Ni or Pt atoms to the surface is not thermodynamically favored in the absence of CO, in contrast to the behavior of Co atoms in the Co–Au system. The phase diagram for the Ni–Au system (Figure 11b) suggests that Ni comprises ~22% (2 out of 9 surface atoms per unit cell) of the surface atoms at room temperature and a CO partial pressure of  $<10^{-10}$  atm. Furthermore, at a CO partial pressure of  $10^{-6}$  atm, a surface with ~44% Ni atoms is stable. In the case of the Pt–Au system (Figure 11c), CO facilitates Pt migration at even lower CO partial pressures than for Ni in the Ni–Au structures. For example, Pt atoms comprise ~44% of the surface atoms at pressures just above  $10^{-10}$  atm, and the surface consists of nearly pure Pt at CO pressures of  $\sim 10^{-3}$  atm. Thus, the thermodynamic driving force for CO to extract metal atoms out of the metal–Au systems is stronger for Pt and Ni compared to Co even though a larger fraction of Co atoms can be found at the bimetallic surface in the absence of CO. These computa-

tional results are consistent with experimental data illustrating that CO-induced diffusion of Pt and Ni occurs more readily than diffusion of Co in the metal–Au clusters.

## DISCUSSION

**Growth, Sintering, and Encapsulation.** Bimetallic Co–Au clusters are formed on  $\text{TiO}_2(110)$  by sequential deposition due to the difference in diffusion rates for Co and Au on the surface. When the less mobile Co atoms are deposited first followed by the more mobile Au atoms, the incoming Au atoms nucleate almost exclusively at the existing Co seed clusters. In general, our group has shown that when there is a significant difference in the diffusion rates for the two metals, bimetallic clusters can be prepared via sequential deposition by depositing the less mobile metal first, followed by the more mobile metal; bimetallic cluster growth was observed for sequential deposition of Pt or Ni seed clusters followed by Au<sup>43,44,47</sup> because Pt and Ni also diffuse less readily on the surface compared to Au. Notably, in the reverse order of deposition of Co deposited on existing Au clusters, Co does not nucleate preferentially at Au sites, and pure Co clusters coexist with clusters that are Au-rich. One major difference between the growth of Co–Au clusters compared to Ni–Au and Pt–Au is that pure Co clusters form many more nucleation sites than the other two metals. Consequently, the cluster density for Co–Au is higher than for the two other bimetallic systems. The high nucleation density for the Co clusters compared to other metals is attributed to the strong Co–titania interfacial energy, as discussed in more detail elsewhere.<sup>104</sup>

For the Co–Au clusters, there is no evidence that the addition of Co suppresses the sintering of the Au clusters, as was previously observed for Pt–Au and Ni–Au clusters on  $\text{TiO}_2(110)$ .<sup>43,44,47</sup> However, the bimetallic Co–Au clusters are smaller than pure Au clusters, both before and after annealing, given that Au nucleates at Co seed clusters and that the slow diffusion of Co on  $\text{TiO}_2$  results in a high cluster density. In the



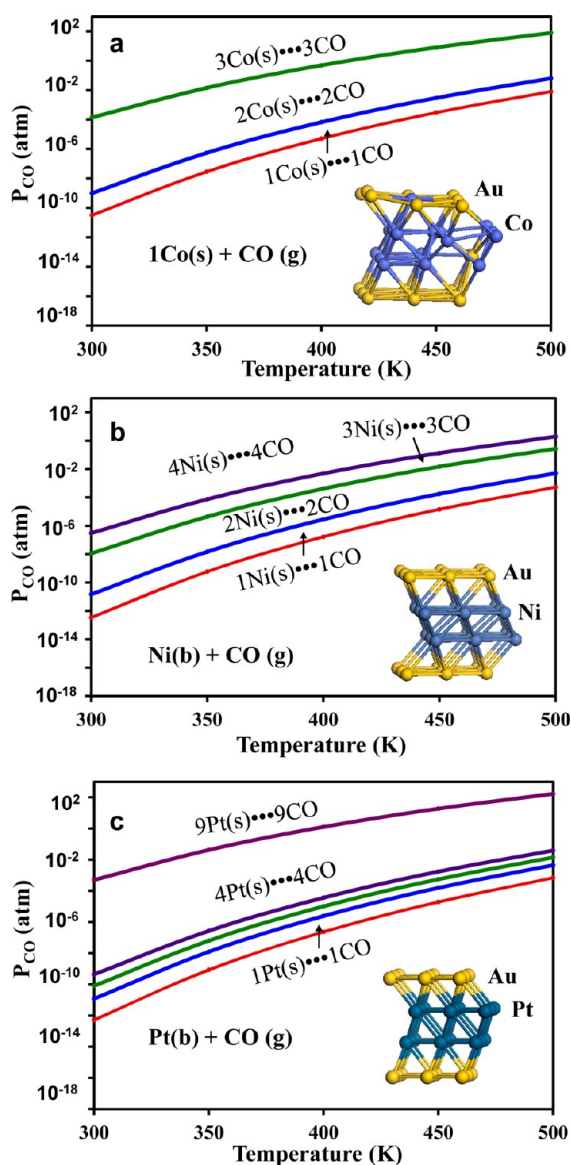


**Figure 11.** Phase diagrams for 50% M/50% Au model surfaces in the presence of CO calculated by constrained ab initio thermodynamics, where M = Co (a), Ni (b), and Pt (c). The most stable structure in the absence of CO is shown in the inset. All other structures are displayed in the Supporting Information.

cluster sintering process, the first step involves detachment of an adatom from an existing cluster and the second step involves diffusion of the atom on the surface to reach another cluster and contribute to its growth. For metals such as Cu, Ni, and Rh on  $\text{TiO}_2(110)$ , previous studies have reported that the rate-limiting step in cluster sintering is adatom detachment rather than adatom diffusion,<sup>85,86</sup> and therefore, the extent of sintering diminishes with increased metal–metal bond strength. This is likely to be the case for Au on  $\text{TiO}_2$  as well because Au diffuses more readily on the surface than Cu, Ni, or Rh; however, because Co diffuses less readily than these other metals, it is possible that adatom diffusion is the rate-limiting step in the sintering of Co clusters. For the Pt–Au clusters, the addition of Pt to Au clusters suppresses sintering because Pt–Pt and Pt–Au bonds are stronger than Au–Au. In the case of Ni, the Ni–Ni bond is only slightly stronger than the Au–Au, and therefore, this effect is much less pronounced. Based on the

heats of sublimation for pure Co (425 kJ/mol)<sup>105,106</sup> and Au (370 kJ/mol),<sup>107</sup> the Co–Co bond is predicted to be slightly stronger than Au–Au. Consequently, the Co clusters should sinter less easily than Au clusters if metal–metal bond breaking is the rate-limiting step, in contrast to the STM results. The facile sintering of the Co clusters at higher temperatures is explained by the enhanced diffusion of Co atoms at 800 K, whereas the Au atoms are already sufficiently mobile, even at room temperature, due to the weaker metal–titania interactions.

In addition to cluster sintering upon annealing, other compositional and structural changes occur at the surfaces of the clusters. The annealing of  $\text{TiO}_2$ -supported Co clusters in UHV results in encapsulation of the clusters by titania, demonstrated by STM and XPS experiments. This same behavior has been previously reported for metals such as Pt, Ni, Pd, and Rh on  $\text{TiO}_2(110)$ ,<sup>45,47,70,72,84,92–95,108</sup> whereas metals like Au and Cu, which do not interact strongly with titania, do not undergo encapsulation.<sup>99,109,110</sup> For the annealed Co–Au clusters on  $\text{TiO}_2$ , the Co becomes encapsulated by titania while the Au remains exposed, resulting in a network of Au–titania sites at the surface. Similarly, studies of Pt–Au and Ni–Au on  $\text{TiO}_2$  annealed in UHV report selective encapsulation of the Pt and Ni at the cluster surface.<sup>43,44,47</sup> A significant difference between the three bimetallic systems is that the clusters containing Co<sup>104</sup> and Ni<sup>111</sup> are encapsulated by stoichiometric titania, whereas the Pt-containing clusters are encapsulated by reduced titania.<sup>45</sup> These surfaces with extended Au–titania interfaces might be useful in increasing the activity of the Au–titania catalysts, assuming active sites are located at the cluster–support interface.<sup>54–56</sup>

#### Adsorbate-Induced Changes in Surface Composition.

In the absence of surface adsorbates, the surface composition of the Co–Au clusters is controlled by the relative surface free energies of Co (1.9 J/m<sup>2</sup>)<sup>87–90</sup> and Au (1.1 J/m<sup>2</sup>).<sup>87,88,90</sup> At bulk Au fractions of >50%, the surface is Au-rich due to the lower surface energy for Au compared to Co. At Au compositions of less than 50%, there is not enough Au present to completely cover the Co seed clusters, and therefore both Co and Au atoms reside at the surface. Likewise, the surfaces of Pt–Au<sup>43,44</sup> and Ni–Au<sup>47</sup> clusters on  $\text{TiO}_2(110)$  are Au-rich, as dictated by the lower surface free energy of Au, and mixed-metal surfaces can be formed for the Pt–Au and Ni–Au clusters at the lower Au fractions, when there is not enough Au to completely cover the clusters. The surface free energies of Ni (1.7 J/m<sup>2</sup>)<sup>87,90,112</sup> and Co are very similar, resulting in nearly identical surface compositions of Au as a function of bulk Au fraction. Given that the Pt surface free energy (2.5 J/m<sup>2</sup>)<sup>113</sup> is the highest of the four metals, it is not surprising that the Au fraction is also the highest at any given bulk Au fraction. In other bimetallic systems, the composition of the surface is determined by the relative surface free energies of the metals, as well as the strain energy arising from a mismatch in atomic sizes; thus, the surfaces of Co–Pt alloys are Pt-rich despite the higher surface free energy of Pt.<sup>114,115</sup> However, for the M–Au systems (M = Pt, Ni, Co) studied here, the relative surface free energies of the metals appear to be the dominant factor.

On Co–Au clusters that are rich in Au at the surface, the adsorption of CO results in activity associated with Co rather than Au, suggesting that CO induces the diffusion of Co to the surface. This effect has also been observed for Pt–Au and Ni–Au clusters on  $\text{TiO}_2(110)$  that are exposed to CO,<sup>44,47</sup> and the extent of CO-induced surface segregation of Pt and Ni is more

extensive than for Co. DFT studies show that metal surface segregation is thermodynamically driven by the formation of strong Co–CO, Pt–CO, and Ni–CO bonds. Furthermore, the calculated phase diagrams for model 50% M/50% Au systems (M = Co, Pt, Ni) with Au–M–M–Au structures demonstrate that for a given pressure of CO, Pt atoms are most easily segregated to the surface, followed by Ni atoms and then Co atoms. This behavior is consistent with the relative strengths of the CO–metal bonds, given that on the pure metal clusters, CO has the lowest desorption temperature on Co, followed by Ni and then Pt, which has the highest desorption temperature.

Adsorbate-induced changes in the composition of other bimetallic surfaces have been experimentally observed in a number of systems where strong metal–adsorbate bonds are formed, particularly with oxygen.<sup>116</sup> For example, Chen and co-workers have investigated monolayer metal films of Ni and Co on Pt(111) by DFT, AES, and HREELS.<sup>117</sup> After annealing these films to 600 K, Ni and Co diffuse into the surface, creating a Pt–M–Pt structure, where M = Ni and Co. However, upon exposure to 400 L of O<sub>2</sub>, surface segregation of Ni or Co occurs at 300–450 K. DFT studies show that oxygen binds more strongly to M–Pt–Pt compared to pure Pt, while oxygen binds less strongly to Pt–M–Pt. Thus, the oxygen-induced diffusion of Ni or Co to the surface is thermodynamically driven by formation of strong metal–oxygen bonds. Varga and co-workers' studies of single-crystal NiPt alloys of varying compositions have reported that exposure of these surfaces to oxygen induces segregation of Ni to the surface,<sup>118</sup> and investigations of a Pt<sub>3</sub>Co(110) alloy showed that oxygen exposure at 573–773 K induces Co segregation to the surface to form Co oxide.<sup>119</sup> Cu<sub>3</sub>Pt(110) alloy surfaces have also undergone Cu surface segregation upon exposure to oxygen at room temperature.<sup>120</sup> Furthermore, studies of PtRh alloy surfaces indicate that exposure to O<sub>2</sub> or NO at >400 K induces Rh diffusion to the surface to make strong Rh–O bonds.<sup>121–124</sup> Similar to the effect of O<sub>2</sub>, exposure to CO induces surface segregation of Pt and Pd at room temperature for AuPt<sup>125</sup> and AuPd<sup>126</sup> systems.

In addition to adsorbate-induced changes in the surfaces of single-crystal alloys and bimetallic films, changes in surface composition have been reported for supported bimetallic clusters. Somorjai and co-workers have shown that the surfaces of supported RhPd and RhPt nanoparticles are controlled by exposure to gases at 573 K and pressures of 100 mtorr. Specifically, reversible changes in surface composition are induced by exposure to an oxidizing (NO or O<sub>2</sub>) or reducing (CO or H<sub>2</sub>) gas environment. Under reducing conditions, Pd or Pt segregates to the surface, but under oxidizing conditions, the surfaces are Rh-rich due to the stability of Rh oxide compared to Pt or Pd oxide.<sup>127,128</sup>

Theoretical studies have also predicted adsorbate-induced changes in bimetallic surface composition. A DFT study of a AuPd alloy surface showed that CO induces Pd segregation to the surface.<sup>129</sup> Likewise, DFT investigations of PtPd and CoCr illustrated that adsorbed oxygen causes enrichment of Pd or Cr atoms at the surface due to the higher oxygen affinity of these metals compared to Pt and Co, respectively.<sup>130</sup> DFT calculations by Balbuena and co-workers reported that surface segregation in bimetallics can be directly correlated with metal–adsorbate bond strengths, and consequently, the surface segregation of metals for Pt<sub>3</sub>M alloys (M = Fe, Co, Ni) is different in vacuum versus in an oxygen environment.<sup>131</sup> For PdAg alloys, Ag prefers to be at the surface under vacuum

conditions, but the strong metal–oxygen bonds favor the diffusion of Pd to the surface in the presence of oxygen.<sup>132</sup> Similarly, the exposure of PdAg alloys to hydrogen induces Pd diffusion to the surface, given that the hydrogen binds more strongly to Pd than Ag.<sup>133</sup>

Diffusion of metal atoms from the bulk to the cluster surface is not expected to be kinetically limited at room temperature, and consequently, the bimetallic surface composition will change if exchange of metal atoms from the bulk to the surface of the clusters is thermodynamically favorable. For example, LEIS experiments for NiAu clusters on TiO<sub>2</sub>(110) showed that the surfaces of 2 ML of Ni deposited on top of 2 ML Au was 80% Au, demonstrating that Au atoms are sufficiently mobile at room temperature to migrate to the cluster surface.<sup>111</sup> Reports of the CO-induced reconstruction of Pt surfaces at room temperature further support the idea that metal atoms are mobile at room temperature.<sup>134–137</sup> As discussed in the preceding paragraphs, many studies of adsorbate-induced surface segregation occur at or near room temperature, which also implies high mobility of atoms at room temperature.

## SUMMARY

Co–Au bimetallic clusters were grown on TiO<sub>2</sub>(110) by sequential deposition of Co, followed by Au. This resulted in preferential nucleation of Au at existing Co clusters due to the slower diffusion of Co on the surface compared to Au. Although the addition of Co to Au clusters does not inhibit cluster sintering, the sizes of the Co–Au clusters both before and after annealing decrease with increasing Co fraction, given the higher nucleation density of Co seed clusters for the larger Co coverages. At Au fractions of >50%, the cluster surface is rich in Au as a result of the higher surface free energy of Au compared to Co. Furthermore, annealing the Co–Au clusters causes encapsulation of the surface Co by TiO<sub>x</sub>, while the Au remains uncovered. Exposure of the Co–Au clusters to CO induces migration of Co from the bulk of the cluster to the surface in order to form the strong Co–CO bonds. This CO-induced metal diffusion has also been observed in Pt–Au and Ni–Au surfaces, but the effect is less pronounced for Co due to the weaker metal–CO bonds. DFT calculations confirm that the surface of the Au clusters should be Au-rich for model bimetallic structures with a 50% Au fraction, and these calculations show that the CO-induced diffusion of metal to the cluster surface follows the trend of Pt > Ni > Co in other metal–Au systems.

## ASSOCIATED CONTENT

### Supporting Information

Average cluster heights and height distributions for Co–Au clusters of various compositions at 295 K and after heating to 800 K; and the most stable structures for the 50%M–50%Au (M = Pt, Ni, Co) bimetallic surfaces used in the DFT calculations for CO adsorption. This material is available free of charge via the Internet at <http://pubs.acs.org>.

## AUTHOR INFORMATION

### Corresponding Author

\*Phone: 803-777-1050. Fax: 803-777-9521. E-mail: [dachen@sc.edu](mailto:dachen@sc.edu).

### Notes

The authors declare no competing financial interest.

## ■ ACKNOWLEDGMENTS

We gratefully acknowledge financial support from the National Science Foundation (CHE 0845788, CBET-0932991, and CBET-0966956) and the Department of Energy, Basic Energy Sciences (DE-FG02-07ER15842). Computational resources were provided by the Pacific Northwest National Laboratory (PNNL, Grant Proposal 34900), National Energy Research Scientific Computing Center (NERSC), Texas Advanced Computing Center (TACC, teragrid), National Institute for Computational Sciences (NICS, teragrid), and the USC Nanocenter.

## ■ REFERENCES

- (1) Khan, N. A.; Chen, J. G. *J. Phys. Chem. B* **2003**, *107*, 4334–4341.
- (2) Kitchin, J. R.; Norskov, J. K.; Barteau, M. A.; Chen, J. G. *Phys. Rev. Lett.* **2004**, *93*, 156801.
- (3) Mavrikakis, M.; Hammer, B.; Norskov, J. K. *Phys. Rev. Lett.* **1998**, *81*, 2819–2822.
- (4) Schlappka, A.; Lischka, M.; Gross, A.; Kasberger, U.; Jakob, P. *Phys. Rev. Lett.* **2003**, *91*, 4.
- (5) Rodriguez, J. A.; Goodman, D. W. *Science* **1992**, *257*, 897–903.
- (6) Kolodziej, J. J.; Pelhos, K.; Abdelrehim, I. M.; Keister, J. W.; Rowe, J. E.; Madey, T. E. *Prog. Surf. Sci.* **1998**, *59*, 117–134.
- (7) Rodriguez, J. A.; Goodman, D. W. *J. Phys. Chem.* **1991**, *95*, 4196–4206.
- (8) Campbell, R. A.; Rodriguez, J. A.; Goodman, D. W.; Ponc, V.; King, D. A.; Niemantsverdriet, H.; Vansanten, R.; Grunert, W.; Chadwick, D.; Bertolini, J. C.; et al. *Stud. Surf. Sci. Catal.* **1993**, *75*, 333–344.
- (9) Rodriguez, J. A.; Campbell, C. T.; Goodman, D. W. *Surf. Sci.* **1994**, *309*, 377–383.
- (10) Watwe, R. M.; Cortright, R. D.; Mavrikakis, M.; Norskov, J. K.; Dumesic, J. A. *J. Chem. Phys.* **2001**, *114*, 4663–4668.
- (11) Zhou, W.-P.; Yang, X.; Vukmirovic, M. B.; Koel, B. E.; Jiao, J.; Peng, G.; Mavrikakis, M.; Adzic, R. R. *J. Am. Chem. Soc.* **2009**, *131*, 12755–12762.
- (12) Kitchin, J. R.; Norskov, J. K.; Barteau, M. A.; Chen, J. G. *J. Chem. Phys.* **2004**, *120*, 10240–10246.
- (13) Tsai, Y. L.; Koel, B. E. *J. Phys. Chem. B* **1997**, *101*, 2895–2906.
- (14) Tsai, Y. L.; Xu, C.; Koel, B. E. *Surf. Sci.* **1997**, *385*, 37–59.
- (15) Panja, C.; Saliba, N. A.; Koel, B. E. *J. Phys. Chem. B* **2001**, *105*, 3786–3796.
- (16) Besenbacher, F.; Chorkendorff, I.; Clausen, B. S.; Hammer, B.; Molenbroek, A. M.; Norskov, J. K.; Stensgaard, I. *Science* **1998**, *279*, 1913–1915.
- (17) Sinfelt, J. H. *Bimetallic Catalysts. Discoveries, Concepts, and Applications*; John Wiley and Sons: New York, 1983.
- (18) Rodriguez, J. A. *Surf. Sci. Rep.* **1996**, *24*, 223–287.
- (19) Campbell, C. *Annu. Rev. Phys. Chem.* **1990**, *41*, 775–837.
- (20) Liu, P.; Norskov, J. K. *Phys. Chem. Chem. Phys.* **2001**, *3*, 3814–3818.
- (21) Sinfelt, J. H. *Acc. Chem. Res.* **1977**, *10*, 15.
- (22) Khan, N. A.; Zellner, M. B.; Chen, J. G. *Surf. Sci.* **2004**, *556*, 87–100.
- (23) Lu, S. L.; Lonergan, W. W.; Bosco, J. P.; Wang, S. R.; Zhu, Y. X.; Xie, Y. C.; Chen, J. G. *J. Catal.* **2008**, *259*, 260–268.
- (24) Hwu, H. H.; Eng, J.; Chen, J. G. *J. Am. Chem. Soc.* **2002**, *124*, 702–709.
- (25) Murillo, L. E.; Goda, A. M.; Chen, J. G. *J. Am. Chem. Soc.* **2007**, *129*, 7101–7105.
- (26) Stottlmyer, A. L.; Ren, H.; Chen, J. G. *Surf. Sci.* **2009**, *603*, 2630–2638.
- (27) Do, P. T. M.; Foster, A. J.; Chen, J.; Lobo, R. F. *Green Chem.* **2012**, *14*, 1388–1397.
- (28) Khan, N. A.; Hwu, H. H.; Chen, J. G. *J. Catal.* **2002**, *205*, 259–265.
- (29) Greeley, J.; Mavrikakis, M. *Nat. Mater.* **2004**, *3*, 810–815.
- (30) Xu, Y.; Ruban, A. V.; Mavrikakis, M. *J. Am. Chem. Soc.* **2004**, *126*, 4717–4725.
- (31) Nilekar, A. U.; Xu, Y.; Zhang, J.; Vukmirovic, M. B.; Sasaki, K.; Adzic, R. R.; Mavrikakis, M. *Top. Catal.* **2007**, *46*, 276–284.
- (32) Friebe, D.; Viswanathan, V.; Miller, D. J.; Anniyev, T.; Ogasawara, H.; Larsen, A. H.; O'Grady, C. P.; Norskov, J. K.; Nilsson, A. *J. Am. Chem. Soc.* **2012**, *134*, 9664–9671.
- (33) Rodriguez, J. A.; Ma, S.; Liu, P.; Hrbek, J.; Evans, J.; Perez, M. *Science* **2007**, *318*, 1757–1760.
- (34) Tang, L. G.; Yamaguchi, D.; Burke, N.; Trimm, D.; Chiang, K. *Catal. Commun.* **2010**, *11*, 1215–1219.
- (35) Chen, D. A.; Ratliff, J. S.; Hu, X.; Gordon, W. O.; Senanayake, S. D.; Mullins, D. R. *Surf. Sci.* **2010**, *604*, 574–587.
- (36) Mullins, D. R.; Robbins, M. D.; Zhou, J. *Surf. Sci.* **2006**, *600*, 1547–1558.
- (37) Senanayake, S. D.; Mullins, D. R. *J. Phys. Chem. C* **2008**, *112*, 9744–9752.
- (38) Senanayake, S. D.; Gordon, W. O.; Overbury, S. H.; Mullins, D. R. *J. Phys. Chem. C* **2009**, *113*, 6208–6214.
- (39) Zhou, J.; Mullins, D. R. *Surf. Sci.* **2006**, *600*, 1540–1546.
- (40) Di Monte, R.; Kaspar, J. *Top. Catal.* **2004**, *28*, 47–57.
- (41) Kaspar, J.; Fornasiero, P.; Graziani, M. *Catal. Today* **1999**, *50*, 285–298.
- (42) Trovarelli, A. *Catal. Rev. Sci. Eng.* **1996**, *38*, 439–520.
- (43) Park, J. B.; Conner, S. F.; Chen, D. A. *J. Phys. Chem. C* **2008**, *112*, 5490–5500.
- (44) Tenney, S. A.; Ratliff, J. S.; He, W.; Roberts, C. C.; Ammal, S. C.; Heyden, A.; Chen, D. A. *J. Phys. Chem. C* **2010**, *114*, 21652–21663.
- (45) Tenney, S. A.; He, W.; Ratliff, J. S.; Mullins, D. R.; Chen, D. A. *Top. Catal.* **2011**, *54*, 42–45.
- (46) Ratliff, J. S.; Tenney, S. A.; Hu, X.; Conner, S. F.; Ma, S.; Chen, D. A. *Langmuir* **2009**, *25*, 216–225.
- (47) Tenney, S. A.; He, W.; Roberts, C. C.; Ratliff, J. S.; Shah, S. I.; Shafai, G. S.; Turkowski, V.; Rahman, T. S.; Chen, D. A. *J. Phys. Chem. C* **2011**, *115*, 11112–11123.
- (48) Haryanto, A.; Fernando, S.; Murali, N.; Adhikari, S. *Energy Fuels* **2005**, *19*, 2098–2106.
- (49) Shabaker, J. W.; Davda, R. R.; Huber, G. W.; Cortright, R. D.; Dumesic, J. A. *J. Catal.* **2003**, *215*, 344–352.
- (50) Haruta, M.; Date, M. *Appl. Catal., A* **2001**, *222*, 427–437.
- (51) Valden, M.; Lai, X.; Goodman, D. W. *Science* **1998**, *281*, 1647–1650.
- (52) Haruta, M. *Catal. Today* **1997**, *36*, 153–166.
- (53) Haruta, M. *Cattech* **2002**, *6*, 102–115.
- (54) Haruta, M.; Tsubota, S.; Kobayashi, T.; Kageyama, H.; Genet, M. J.; Delmon, B. *J. Catal.* **1993**, *144*, 175–192.
- (55) Green, I. X.; Tang, W.; Neurock, M.; Yates, J. R. *Science* **2011**, *333*, 736–739.
- (56) Molina, L. M.; Hammer, B. *Appl. Catal., A* **2005**, *291*, 21–31.
- (57) Batista, M. S.; Santos, R. K. S.; Assaf, E. M.; Assaf, J. M.; Ticianelli, E. A. *J. Power Sources* **2003**, *124*, 99–103.
- (58) Haga, F.; Nakajima, T.; Yamashita, K.; Mishima, S.; Suzuki, S. *Nippon Kagaku Kaishi* **1997**, 33–36.
- (59) Llorca, J.; Homs, N.; Sales, J.; de la Piscina, P. R. *J. Catal.* **2002**, *209*, 306–317.
- (60) Haga, F.; Nakajima, T.; Miya, H.; Mishima, S. *Catal. Lett.* **1997**, *48*, 223–227.
- (61) Haga, F.; Nakajima, T.; Yamashita, K.; Mishima, S. *React. Kinet. Catal. Lett.* **1998**, *63*, 253–259.
- (62) Jalama, K.; Coville, N. J.; Hildebrandt, D.; Glasser, D.; Jewell, L. L.; Anderson, J. A.; Taylor, S.; Enache, D.; Hutchings, G. J. *Top. Catal.* **2007**, *44*, 129–136.
- (63) Jalama, K.; Coville, N. J.; Xiong, H. F.; Hildebrandt, D.; Glasser, D.; Taylor, S.; Carley, A.; Anderson, J. A.; Hutchings, G. J. *Appl. Catal., A* **2011**, *395*, 1–9.
- (64) Leite, L.; Stonkus, V.; Ilieva, L.; Plyasova, L.; Tabakova, T.; Andreeva, D.; Lukevics, E. *Catal. Commun.* **2002**, *3*, 341–347.



- (65) Li, J. L.; Jacobs, G.; Zhang, Y. Q.; Das, T.; Davis, B. H. *Appl. Catal., A* **2002**, 223, 195–203.
- (66) Jacobs, G.; Das, T. K.; Zhang, Y. Q.; Li, J. L.; Racoillet, G.; Davis, B. H. *Appl. Catal., A* **2002**, 233, 263–281.
- (67) Yeo, B. S.; Bell, A. T. *J. Am. Chem. Soc.* **2011**, 133, 5587–5593.
- (68) Mennemann, C.; Claus, P. *Catal. Lett.* **2010**, 134, 31–36.
- (69) Park, J. B.; Ratliff, J. S.; Ma, S.; Chen, D. A. *J. Phys. Chem. C* **2007**, 111, 2165–2176.
- (70) Zhou, J.; Ma, S.; Kang, Y. C.; Chen, D. A. *J. Phys. Chem. B* **2004**, 108, 11633–11644.
- (71) Tenney, S. A.; Cagg, B. A.; Levine, M. S.; He, W.; Manandhar, K.; Chen, D. A. *Surf. Sci.* **2012**, 606, 1233–1243.
- (72) Ozturk, O.; Park, J. B.; Black, T. J.; Rodriguez, J. A.; Hrbek, J.; Chen, D. A. *Surf. Sci.* **2008**, 602, 3077–3088.
- (73) Varazo, K.; Parsons, F. W.; Ma, S.; Chen, D. A. *J. Phys. Chem. B* **2004**, 108, 18274–18283.
- (74) Illingworth, A.; Zhou, J.; Ozturk, O.; Chen, D. A. *J. Vac. Sci. Technol., B* **2004**, 22, 2552.
- (75) Ratliff, J. S. The Morphology and Catalytic Activity of Bimetallic Nanoclusters Supported on TiO<sub>2</sub>(110). *Ph.D. Dissertation*, University of South Carolina, Columbia, SC, 2009.
- (76) Jak, M. J.; Konstapel, C.; van Kreuningen, A.; Verhoeven, J.; van Gastel, R.; Frenken, J. W. M. *Surf. Sci.* **2001**, 494, 43–52.
- (77) Kresse, G.; Furthmüller, J. *Phys. Rev. B* **1996**, 54, 11169–11186.
- (78) Kresse, G.; Furthmüller, J. *Comput. Mater. Sci.* **1996**, 6, 15–50.
- (79) Kresse, G.; Hafner, J. *Phys. Rev. B* **1993**, 47, 558–561.
- (80) Perdew, J. P.; Burke, K.; Ernzerhof, M. *Phys. Rev. Lett.* **1996**, 77, 3865–3868.
- (81) Hammer, B.; Hansen, L. B.; Norskov, J. K. *Phys. Rev. B* **1999**, 59, 7413–7421.
- (82) Methfessel, M.; Paxton, A. T. *Phys. Rev. B* **1989**, 40, 3616–3621.
- (83) Makov, G.; Payne, M. C. *Phys. Rev. B* **1995**, 51, 4014–4022.
- (84) Ozturk, O.; Ma, S.; Park, J. B.; Ratliff, J. S.; Zhou, J.; Mullins, D. R.; Chen, D. A. *Surf. Sci.* **2007**, 601, 3099–3113.
- (85) Park, J. B.; Ratliff, J. S.; Ma, S.; Chen, D. A. *Surf. Sci.* **2006**, 600, 2913–2923.
- (86) Zhou, J.; Kang, Y. C.; Chen, D. A. *Surf. Sci.* **2003**, 537, L429–L434.
- (87) Chatain, D.; Rivollet, I.; Eustathopoulos, N. *J. Chim. Phys. Phys.-Chim. Biol.* **1986**, 83, 561.
- (88) Sangiorgi, R.; Muolo, M. L.; Chatain, D.; Eustathopoulos, N. *J. Am. Ceram. Soc.* **1988**, 71, 742.
- (89) Chatain, D.; Rivollet, I.; Eustathopoulos, N. *J. Chim. Phys. Phys.-Chim. Biol.* **1987**, 84, 201–203.
- (90) Campbell, C. T. *Surf. Sci. Rep.* **1997**, 27, 1–111.
- (91) *Binary Alloy Phase Diagrams*, 2nd ed.; Massalski, T. B., International, A., Okamoto, H., Eds.; ASM International: Materials Park, OH, 1990.
- (92) Pesty, F.; Steinrück, H.-P.; Madey, T. E. *Surf. Sci.* **1995**, 339, 83–95.
- (93) Bowker, M.; Fourre, E. *Appl. Surf. Sci.* **2008**, 254, 4225–4229.
- (94) Bennett, R. A.; Stone, P.; Bowker, M. *Catal. Lett.* **1999**, 59, 99–105.
- (95) Bowker, M.; Stone, P.; Morrall, P.; Smith, R.; Bennett, R.; Perkins, N.; Kvon, R.; Pang, C.; Fourre, E.; Hall, M. J. *Catal.* **2005**, 234, 172–181.
- (96) Tauster, S. J.; Fung, S. C.; Garten, R. L. *J. Am. Chem. Soc.* **1978**, 100, 170–175.
- (97) Tauster, S. J. *Acc. Chem. Res.* **1987**, 20, 389–394.
- (98) Tauster, S. J.; Fung, S. C.; Baker, R. T. K.; Horsley, J. A. *Science* **1981**, 211, 1121–1125.
- (99) Diebold, U.; Pan, J. M.; Madey, T. E. *Surf. Sci.* **1995**, 333, 845–854.
- (100) Pan, J. M.; Madey, T. E. *J. Vac. Sci. Technol., A* **1993**, 11, 1667–1674.
- (101) Feldman, L. C.; Meyer, J. W. *Fundamentals of Surface and Thin Film Analysis*; P T R Prentice-Hall, Inc.: Englewood Cliffs, NJ, 1986.
- (102) *Surface Analysis: The Principal Techniques*; Vickerman, J. C., Ed.; John Wiley and Sons: New York, 1997.
- (103) Bridge, M. E.; Comrie, C. M.; Lambert, R. M. *Surf. Sci.* **1977**, 67, 393–404.
- (104) Galhenage, R. P.; Yan, H.; Park, N.; Henkelman, G.; Albrecht, P.; Mullins, D. R.; Chen, D. A., in preparation.
- (105) NIST-JANAF Thermochemical Tables, *J. Phys. Chem. Ref. Data*, 4th ed.; Chase, M. W., Ed.; American Institute of Physics: Melville, NY, 1998; Vol. Monograph 9, pp 1–1951.
- (106) Dean, J. A. *Lange's Handbook of Chemistry*, 15th ed.; McGraw-Hill: New York, 1998.
- (107) Hildenbrand, D. L.; Hall, W. F. *J. Phys. Chem.* **1962**, 66, 754–755.
- (108) Baker, T. A.; Kaxiras, E.; Friend, C. M. *Top. Catal.* **2010**, 53, 365–377.
- (109) Diebold, U.; Pan, J. M.; Madey, T. E. *Phys. Rev. B* **1993**, 47, 3868–3876.
- (110) Zhang, L.; Persaud, R.; Madey, T. E. *Phys. Rev. B* **1997**, 56, 10549–10557.
- (111) Jacobsen, C. J. H.; Dahl, S.; Clausen, B. S.; Bahn, S.; Logadottir, A.; Norskov, J. K. *J. Am. Chem. Soc.* **2001**, 123, 8404–8405.
- (112) Peden, C. H. F.; Kidd, K. B.; Shinn, N. D. *J. Vac. Sci. Technol., A* **1991**, 9, 1518.
- (113) Jiang, Q.; Lu, H. M.; Zhao, M. J. *Phys.: Condens. Matter* **2004**, 16, 521–530.
- (114) Nilekar, A. U.; Sasaki, K.; Farberow, C. A.; Adzic, R. R.; Mavrikakis, M. *J. Am. Chem. Soc.* **2011**, 133, 18574–18576.
- (115) Gauthier, Y.; Baudoin-Savois, R.; Bugnard, J. M.; Hebenstreit, W.; Schmid, M.; Varga, P. *Surf. Sci.* **2000**, 466, 155–166.
- (116) Menning, C. A.; Chen, J. G. G. *J. Chem. Phys.* **2009**, 130, 174709.
- (117) Menning, C. A.; Hwu, H. H.; Chen, J. G. G. *J. Phys. Chem. B* **2006**, 110, 15471–15477.
- (118) Weigand, P.; Novacek, P.; van Husen, G.; Neidhart, T.; Varga, P. *Surf. Sci.* **1992**, 269–270, 1129–1134.
- (119) An, K. S.; Kimura, A.; Ono, K.; Kamakura, N.; Kakizaki, A.; Park, C. Y.; Tanaka, K. *Surf. Sci.* **1998**, 401, 336–343.
- (120) Shen, Y. G.; O'Connor, D. J.; Wandelt, K. *Surf. Sci.* **1998**, 410, 1–14.
- (121) Tanaka, K. I.; Sasahara, A. *J. Mol. Catal. A: Chem.* **2000**, 155, 13–22.
- (122) Hirano, H.; Yamada, T.; Tanaka, K.; Siera, J.; Nieuwenhuys, B. E. *Surf. Sci.* **1989**, 222, L804–L808.
- (123) Tamura, H.; Tanaka, K. *Langmuir* **1994**, 10, 4530–4533.
- (124) Matsumoto, Y.; Okawa, Y.; Fujita, T.; Tanaka, K. *Surf. Sci.* **1996**, 355, 109–114.
- (125) Bouwman, R.; Sachtler, W. M. H. *J. Catal.* **1970**, 19, 127–139.
- (126) Gao, F.; Wang, Y. L.; Goodman, D. W. *J. Phys. Chem. C* **2009**, 113, 14993–15000.
- (127) Tao, F.; Grass, M. E.; Zhang, Y. W.; Butcher, D. R.; Aksoy, F.; Aloni, S.; Altöe, V.; Alayoglu, S.; Renzas, J. R.; Tsung, C. K.; et al. *J. Am. Chem. Soc.* **2010**, 132, 8697–8703.
- (128) Tao, F.; Grass, M. E.; Zhang, Y. W.; Butcher, D. R.; Renzas, J. R.; Liu, Z.; Chung, J. Y.; Mun, B. S.; Salmeron, M.; Somorjai, G. A. *Science* **2008**, 322, 932–934.
- (129) Soto-Verdugo, V.; Metiu, H. *Surf. Sci.* **2007**, 601, 5332–5339.
- (130) Dianat, A.; Zimmermann, J.; Seriani, N.; Bobeth, M.; Pompe, W.; Ciacchi, L. C. *Surf. Sci.* **2008**, 602, 876–884.
- (131) Ma, Y. G.; Balbuena, P. B. *Surf. Sci.* **2009**, 603, 349–353.
- (132) Kitchin, J. R.; Reuter, K.; Scheffler, M. *Phys. Rev. B* **2008**, 77, 075437.
- (133) Lovvik, O. M.; Opalka, S. M. *Surf. Sci.* **2008**, 602, 2840–2844.
- (134) Gritsch, T.; Coulman, D.; Behm, R. J.; Ertl, G. *Phys. Rev. Lett.* **1989**, 63, 1086–1089.
- (135) Thiel, P. A.; Behm, R. J.; Norton, P. R.; Ertl, G. *J. Chem. Phys.* **1983**, 78, 7448–7458.
- (136) Tao, F.; Dag, S.; Wang, L. W.; Liu, Z.; Butcher, D. R.; Salmeron, M.; Somorjai, G. A. *Nano Lett.* **2009**, 9, 2167–2171.
- (137) Tao, F.; Dag, S.; Wang, L. W.; Liu, Z.; Butcher, D. R.; Bluhm, H.; Salmeron, M.; Somorjai, G. A. *Science* **2010**, 327, 850–853.